Journal Pre-proof

Scaling laws and the left main coronary artery bifurcation. A combination of geometric and simulation analyses

Pablo J. Blanco, Gabriela H. Vargas dos Santos, Carlos A. Bulant, Alonso M. Alvarez, Fredric A.P. Oliveira, Gabriella Cunha-Lima, Pedro A. Lemos

PII: S1350-4533(21)00101-6
DOI: https://doi.org/10.1016/j.medengphy.2021.08.011
Reference: JJBE 3701

To appear in: *Medical Engineering and Physics*

Received date: 18 January 2021
Revised date: 25 August 2021
Accepted date: 31 August 2021

Please cite this article as: Pablo J. Blanco, Gabriela H. Vargas dos Santos, Carlos A. Bulant, Alonso M. Alvarez, Fredric A.P. Oliveira, Gabriella Cunha-Lima, Pedro A. Lemos, Scaling laws and the left main coronary artery bifurcation. A combination of geometric and simulation analyses, *Medical Engineering and Physics* (2021), doi: https://doi.org/10.1016/j.medengphy.2021.08.011

HIGHLIGHTS

- Comparison of in-vivo coronary vessel diameter with existing scaling laws.
- Assessment of different power-law criteria in the characterization of blood flow models.
- Novel approach to enforce matching between averaged wall shear stresses in branching vessels.
- Huo-Kassab's criterion results in improved shear stress balancing between branching vessels.

Scaling laws and the left main coronary artery bifurcation. A combination of geometric and simulation analyses

Pablo J. Blanco[a,e], Gabriela H. Vargas dos Santos[b], Carlos A. Bulant[c,e], Alonso M. Alvarez[a,e], Fredric A.P. Oliveira[b], Gabriella Cunha-Lima[b], Pedro A. Lemos[b,d,e,*]

[a]*National Laboratory for Scientific Computing, Av. Getúlio Vargas 333, 25651-075, Petrópolis, Brazil*
[b]*Hospital Israelita Albert Einstein. São Paulo, Brazil.*
[c]*National Scientific and Technical Research Council , CONICET and National University of the Center, Tandil, Argentina*
[d]*Department of Interventional Cardiology, Heart Institute (InCor) and the University of São Paulo Medical School, 05403-904, São Paulo, Brazil*
[e]*National Institute of Science and Technology in Medicine Assisted by Scientific Computing, Petrópolis, Brazil*

Abstract

The geometry of coronary arteries is believed to play the role as an atherosclerotic risk factor on its own. The full characterization of the normal coronary network has been reported in the literature. Reports on the integration of geometry and functional data for normal coronary vessels started to proliferate more recently. In this work, we analyze and integrate the geometric data retrieved from angiography images of the left main coronary bifurcation in angiographically normal patients and hemodynamic data generated from blood flow models to analyze the role of allometric laws and the connection between flow distribution and wall shear stress loads on the left anterior descending and left circumflex arteries. This in-silico study contributes to the characterization of normal coronary anatomy and its impact on the hemodynamic shear stresses acting over the vessel wall, shedding light on the impact of geometry-based

*Corresponding author
Email address: `pedro.lemos@atscien.com` (Pedro A. Lemos)

versus simulation-based hypotheses to define boundary conditions for numerical simulations. We discuss the role of the wall shear stress corresponding to scenarios adopted by the scientific community and the ones proposed in this study. For the simulation-based hypothesis, we propose an iterative strategy to define boundary conditions at the main left coronary bifurcation, such that wall shear stresses are matched between the left descending and left circumflex arteries. From this study, we conclude that a one-fits-all power law exponent of 7/3 results in an good trade-off between computational cost and wall shear stress balance between daughter vessels.

Keywords: Coronary arteries, Allometric laws, Angiography, Vascular geometry, Blood flow, Simulation

WORD COUNT: 4418

---

1. Introduction

Since the emergence of the concept of geometric risk factors in atherosclerosis research [1], the study of arterial geometry in the coronary network has received attention along the years [2, 3, 4]. Knowledge of arterial geometry is vital for any image-based diagnostic protocol [5], and also for therapeutic planning concerning stent deployment [6, 7, 8].

In the field of computational hemodynamics, the importance of the proper characterization of the arterial geometry is twofold:

(a) the macro-scale geometry (observable vessels from medical images) is used to define the vascular domain where the blood flow is to be analyzed from computer simulations;

(b) the same arterial geometry is employed as a surrogate of the downstream micro-scale vasculature (peripheral vessels not visible in medical images), to define boundary conditions for simulations.

Particularly, the latter case is crucial because the boundary conditions determine the way in which blood flow is regionally distributed among the vascular territories composing the myocardium wall. This greatly impacts the performance of simulation-based diagnosis procedures, such as non-invasive fractional flow reserve (FFR) [9, 10].

Investigation of coronary arterial branching has been matter of intensive research, and different scaling laws have been derived to provide a characterization of the fractal nature of arterial bifurcations in the coronary network. Since Murray's landmark contribution [11], numerous authors have proposed extensions and validations of Murray's law for different organs [12, 13, 14, 15, 16] and also in the case of stenotic disease [17]. Modeling the geometry of coronary networks allowed the development of massive coronary networks [18], leading to the development of complex multi-scale models bridging the large coronary vessels to the tissue microcirculation [19].

Integration of geometric analysis and blood flow simulation started to proliferate more recently. The impact of boundary conditions on the wall shear stress was studied previously [20], rising concerns about the applicability of the Murray's law to define boundary conditions. These findings are complementary to the evidence that deviation from Murray's law is associated to plaque composition [21]. Going back to the field of blood flow simulations, the impact of boundary conditions on the blood flow distribution, using 1D and 3D models, and its effect in the computation of flow-derived quantities was acknowledged in [22, 23].

Nevertheless, the interplay between geometry and boundary conditions in a semi-controled scenario can provide insight about the role of macro-scale geometry and micro-scale vasculature. In this work, we investigate the relation between arterial geometry and wall shear stresses (WSS) determined from blood flow simulations. We assessed angiographic images from 50 angiographically normal patients and extracted the diameters of the left main (LM), left anterior descending (LAD) and left circumflex (LCX) vessels. With these data, several simulation scenarios are considered to study the WSS in both branching vessels (LAD/LCX). The strategies employed to define boundary conditions are based on either conventional power laws, or in geometric-based and simulation-based criteria. For the simulation-based criteria, we propose an optimality criterion by which the boundary conditions are adapted to match the averaged WSS in the LAD and LCX. This perfect WSS balance is the main theoretical outcome of Murray's law. We will see that the Murray's law does not deliver such a perfect matching as a consequence of the three-dimensional nature of blood flow. Finally, we quantify and analyze the deviation of such an optimal condition from Murray's law and discuss on the practical aspects of alternative choices to reduce the mismatch in the WSS between daughter vessels.

2. Materials and methods

2.1. Study format and patient population

Cases were retrospectively selected from a cohort of patients who underwent invasive angiography for stratification of suspected coronary disease since 2017. Patients were excluded if presenting: i) previous coronary invasive treatment (either surgical or percutaneous); ii) any angiographic abnormality (i.e. luminal irregularities, stenotic, and/or ectatic-aneurysmatic disease); iii) trifurcated left main coronary; iv) absent or short (i.e. < 5 mm in length) left main coronary; v) absent or short (i.e. < 5 mm in length) proximal left circumflex or left anterior descending arteries. Finally, only patients with adequate images for optimal quantitative coronary angiography (QCA) were ultimately included (i.e. two orthogonal views, no foreshortening, no crossing branches, visible angiographic catheter for calibration) (see top panels in Figure 1).

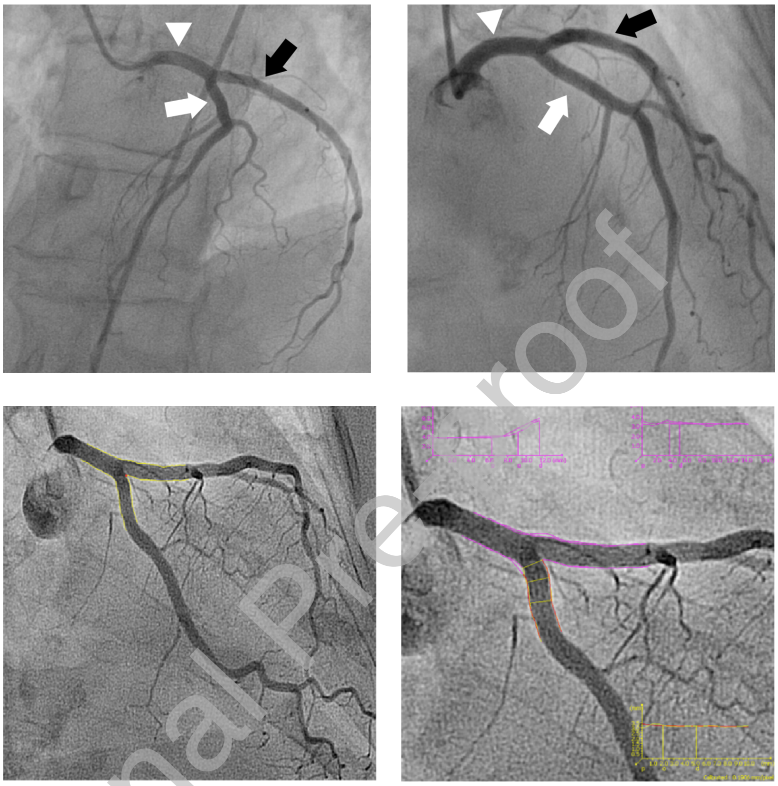

Figure 1: Top: Left main coronary artery in two orthogonal views (cranial left anterior oblique and cranial right anterior oblique). The left main coronary (white arrow head) is bifurcated and originates the left anterior descending (white arrow) and the left circumflex arteries (black arrow). Note the absence of coronary obstructions, the long tubular segments of all target segments. Bottom: Segment window to extract diameter measurements.

A minimal sample size of 45 cases was calculated, aiming to allow to test the hypothesis that any predicted vessel size (e.g. side branch size predicted by Murray's law) would correlate with the actual vessel measurements with a correlation coefficient (r) of least 0.7, assuming a two-tailed alpha of 0.001 (i.e. 0.1% probability of a Type I error [rejecting the null hypothesis when it is in fact correct]) and a beta of 0.01 (i.e. 1% probability of a Type II error [accepting

Male, [%]	62
Age [y]	61.6 ± 12.1
Diabetes	18.0
Hypertension	42.0
Body mass index [kg/m^2]	28.8 ± 4.5
Ejection fraction, [%]	63.5 ± 0.1
Left ventricular mass index, [g/m^2]	92.3 ± 26.1
Right/Left/Co-dominance	47/2/1

Table 1: Demographic characteristics ($n = 50$ patients). Numbers are proportions or mean $\pm$ standard deviation.

the null hypothesis when it is in fact false]). Ultimately, therefore, a total of 50 consecutive cases were included and comprised the present study population (see Table 1).

2.2. Quantitative coronary angiography

The mean diameter of the tubular portions of the left main, left anterior descending artery and circumflex artery were measured using a dedicated QCA software (QangioXA 7.3, by Medis medical imaging systems BV, Leiden, The Netherlands). All vessels were analyzed in two orthogonal views. From each view, the spatial window corresponding to each segment (LM, LAD and LCX) were delimited, as seen in the bottom panel of Figure 1, and the vessel diameter in each segment was averaged over a spatial window of 5 mm. The final vessel diameter that we consider for the present study was obtained by taking the average between the values of the two angiographic views. The accuracy and precision of the measurements (i.e. the mean difference and the standard deviation of repeated QCA measurements performed in a session $>$ 1 month apart) were assessed in a sample of ten cases and were 0.01 mm and 0.17 mm, respectively.

Vessel diameters are denoted by D_{LM}, D_{LAD} and D_{LCX} for the left main, left anterior descending and left circumflex arteries, correspondingly.

2.3. Allometric laws

Murray's law [11] establishes that, at a bifurcation, the diameter of the parent vessel is related to the diameters of both daughter vessels through a cubic power law. Other alternative allometric laws were proposed in the literature, such as the Huo-Kassab's and the Finet's laws [24]. For the case of the left main bifurcation, power laws are usually encountered in the following format

$$D_{\mathrm{LM}}^{\gamma} = D_{\mathrm{LAD}}^{\gamma} + D_{\mathrm{LCX}}^{\gamma}, \tag{1}$$

where D_{LM}, D_{LAD} and D_{LCX} are the LM, LAD and LCX diameters, respectively. Then, for Murray's law we have $\gamma_{\mathrm{M}} = 3$, and for Huo-Kassab's law it is $\gamma_{\mathrm{HK}} = 7/3 = 2.333$.

In this work we consider two additional power laws, called geometry-specific (GS) and simulation-specific (SS) power laws. In the geometry-specific law the exponent γ_{GS} is computed such that the power law (1) holds for the specific vessel diameters $D_{\mathrm{LM}}, D_{\mathrm{LAD}}, D_{\mathrm{LCX}}$ measured for each patient. In the simulation-specific law the exponent γ_{SS} is computed such that the flow distribution renders the same WSS in both daughter vessels.

Note that a patient-specific triple $(D_{\mathrm{LM}}, D_{\mathrm{LAD}}, D_{\mathrm{LCX}})$, does not necessarily verify the power law (1), for some exponent γ. In those cases, the Murray ratio, defined in [21], measures the deviation from the power law format, this is

$$\mathsf{R}_{\mathrm{C}} = \frac{D_{\mathrm{LM}}^{\gamma_{\mathrm{C}}}}{D_{\mathrm{LAD}}^{\gamma_{\mathrm{C}}} + D_{\mathrm{LCX}}^{\gamma_{\mathrm{C}}}} \quad \mathrm{C} \in \{\mathrm{M}, \mathrm{HK}, \mathrm{SS}\}. \tag{2}$$

Note that, by definition, $\mathsf{R}_{\mathrm{GS}} = 1$ for all patients.

From the measured diameters we also compute the asymmetry ratio defined as (see [25])

$$\zeta = \left(\frac{D_{\mathrm{LCX}}}{D_{\mathrm{LAD}}}\right)^2. \tag{3}$$

2.4. Computational hemodynamics

2.4.1. Phantom model generation

Phantom geometries are constructed based in the anatomical information provided in [26], where morphological information from 217 patient-specific left-main coronary bifurcations were analyzed to describe their shape variations (diameters and angles). A model centerline is built based on the data reported in that work: LAD and LCX are considered to be coplanar segments with a separation angle of $\beta = \beta_1 + \beta_2 = 75.2°$, LM segment forms an angle $\alpha = 8°$ with the LAD-LCX plane and the angle between LM and LAD branches is $\delta = 138.6°$. Straight segments have the same length $L = 3$ cm. Tubular surfaces are generated on top of the centerline, from a given vessel diameter, following the pipeline described in [27]. Tubes are considered to be straight and the junction is reconstructed enforcing geometrical smoothness, naturally required in this kind of applications. Definition of model geometry is shown in Figure 2. In this work, such a strategy was applied to the sample of 50 geometries employing the measurements of LM, LAD and LCX arterial diameters.

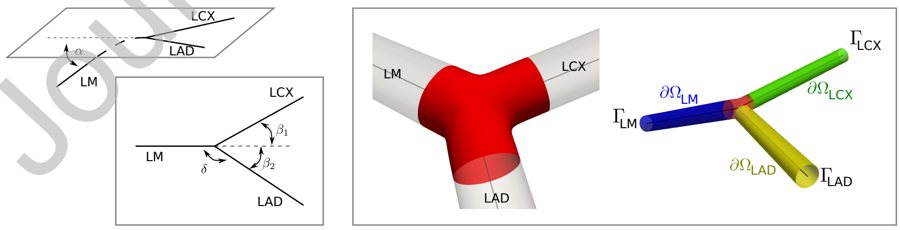

Figure 2: Left: Definition of the LM-LAD-LCX geometry for $\alpha = 8°, \beta_1 = 33.8°, \beta_2 = 41.4°, \delta = 138.6°$. Right: Reconstructed surface for a specific case from the patient sample. Inlet/Outlet boundaries are $\Gamma_{\mathrm{LM}}, \Gamma_{\mathrm{LAD}}, \Gamma_{\mathrm{LCX}}$. Over the endothelial boundaries colored regions indicate the part of the boundaries $\partial\Omega_{\mathrm{LM}}, \partial\Omega_{\mathrm{LAD}}, \partial\Omega_{\mathrm{LCX}}$ where the average wall shear stress is computed.

2.4.2. Blood flow simulation

For each phantom coronary, denoted as Ω, the equations from fluid mechanics are approximately solved. Specifically, we consider the flow to be incompressible, and the regime to be steady-state. This assumption is reasonable because we are interested in the per-segment average WSS, and previous works [28, 29] showed that for average quantities the steady-state assumption yields satisfactory results. Also, the arterial wall is considered to be rigid, and lateral flow condition is no-slip. The problem amounts to find the velocity $\mathbf{u}$ and the pressure p fields, such that

$$\begin{cases} \rho(\nabla\mathbf{u})\mathbf{u} - \mu\triangle\mathbf{u} + \nabla p = \mathbf{0} & \text{in } \Omega, \\ \text{div } \mathbf{u} = 0 & \text{in } \Omega, \\ \mathbf{u} = \mathbf{0} & \text{on } \Gamma_{\mathrm{W}}, \\ \int_{\Gamma_{\mathrm{LM}}} \mathbf{u}\cdot\mathbf{n}d\Gamma = Q_{\mathrm{LM}} & \text{on } \Gamma_{\mathrm{LM}}, \\ -p\mathbf{n} + \mu(\nabla\mathbf{u} + \nabla\mathbf{u}^T)\mathbf{n} = -R_{\mathrm{A}}Q_{\mathrm{A}}\mathbf{n} & \text{on } \Gamma_{\mathrm{A}} \ \mathrm{A} \in \{\mathrm{LAD}, \mathrm{LCX}\}, \end{cases} \tag{4}$$

where ρ and μ are the fluid density and dynamic viscosity, respectively, Γ_{W} is the lateral wall boundary, Γ_{LM} is the inlet boundary at the left main artery, and Γ_{LAD} and Γ_{LCX} are the corresponding outlet boundaries at the LAD and LCX vessels, respectively. At the inlet we prescribe the flow rate to be Q_{LM}, while the outlet boundary conditions model the pressure-flow linear relation (resistance relation) at each downstream vasculature. Hence, R_{LAD} and R_{LCX} model the hemodynamic behavior of the corresponding peripheral territories. The value of these resistances is as given in (12). Also, note that

$$Q_{\mathrm{A}} = \int_{\Gamma_{\mathrm{A}}} \mathbf{u}\cdot\mathbf{n}d\Gamma \qquad \mathrm{A} \in \{\mathrm{LAD}, \mathrm{LCX}\}. \tag{5}$$

Finally, the strategy for the definition of R_{LAD} and R_{LCX} is explained in next section.

The system of equations in (4) includes the so-called defective boundary conditions [30, 31]. This arises from the fact that the velocity profile is not known a priori at $\Gamma_{\mathrm{LM}}, \Gamma_{\mathrm{LAD}}, \Gamma_{\mathrm{LCX}}$. Thus, the boundary conditions involve a constraint over the velocity field. In the present work, we assume that the normal component of the stress tensor is uniform in the corresponding boundary. Moreover, a Lagrange multiplier approach is considered to enforce the constraint at the inlet. The resulting variational equation reads: find $(\mathbf{u}, p, \lambda_{\mathrm{LM}}) \in \mathbf{H}^1_{0,\Gamma_{\mathrm{W}}}(\Omega) \times L^2(\Omega) \times \mathbb{R}$ such that

$$\begin{aligned}
\int_{\Omega} \big(\rho(\nabla\mathbf{u})\mathbf{u}\cdot\hat{\mathbf{u}} + 2\mu\nabla^s\mathbf{u}\cdot\nabla^s\hat{\mathbf{u}} - p\,\mathrm{div}\,\hat{\mathbf{u}} - \hat{p}\,\mathrm{div}\,\mathbf{u}\big)d\Omega& \\
+ \int_{\Gamma_{\mathrm{LAD}}} R_{\mathrm{LAD}}\left(\int_{\Gamma_{\mathrm{LAD}}} \mathbf{u}\cdot\mathbf{n}d\Gamma\right)\mathbf{n}\cdot\hat{\mathbf{u}}d\Gamma& \\
+ \int_{\Gamma_{\mathrm{LCX}}} R_{\mathrm{LCX}}\left(\int_{\Gamma_{\mathrm{LCX}}} \mathbf{u}\cdot\mathbf{n}d\Gamma\right)\mathbf{n}\cdot\hat{\mathbf{u}}d\Gamma& \\
+ \left(\int_{\Gamma_{\mathrm{LM}}} \mathbf{u}\cdot\mathbf{n}d\Gamma - Q_{\mathrm{LM}}\right)\hat{\lambda}_{\mathrm{LM}} + \int_{\Gamma_{\mathrm{LM}}} \lambda_{\mathrm{LM}}\mathbf{n}\cdot\hat{\mathbf{u}}d\Gamma = 0& \\
\forall(\hat{\mathbf{u}}, \hat{p}, \hat{\lambda}_{\mathrm{LM}}) \in \mathbf{H}^1_{0,\Gamma_{\mathrm{W}}}(\Omega) \times L^2(\Omega) \times \mathbb{R}& \qquad (6)
\end{aligned}$$

where ∇^s is the symmetric gradient operator, $L^2(\Omega)$ is the space of square integrable functions in Ω and $\mathbf{H}^1_{0,\Gamma_{\mathrm{W}}}(\Omega)$ is the space of square integrable vector functions in Ω with square integrable gradients in Ω, and whose trace is null over the lateral boundary Γ_{W}.

Numerical approximation of the variational form (6) is performed using the Transversally Enriched Pipe Element Method (TEPEM). This technique is an element-based approach tailored to computational hemodynamics applications. The geometry is discretized into 4 704 elements, of axial length $h = 0.1\,\mathrm{cm}$, and approximately 129K degrees of freedom. Overall, 200 simulations were performed. Each simulation was performed in a personal computer (with 8 processors) and solving the flow problem in a mean time of 4 minutes. The reader will find the technical aspects of the numerical methodology in [27].

2.4.3. Model parameters and data processing

We consider $\rho = 1.04$ g/cm^3, $\mu = 4$ cP. The incoming flow rate Q_{LM} is computed following [32], taking into consideration arterial dominance. Thus, we have $Q_{\mathrm{LM}} = 2.60$ ml/s for right dominant coronary circulation, and $Q_{\mathrm{LM}} = 3.38$ ml/s for left dominant and co-dominant coronary circulations.

Resistances R_{LAD} and R_{LCX} are defined as a function of a power law with exponent γ. Assuming a power law relation between flow rate and arterial diameter we have

$$Q_{\mathrm{A}} = \sigma D_{\mathrm{A}}^{\gamma} \quad \mathrm{A} \in \{\mathrm{LAD}, \mathrm{LCX}\}. \tag{7}$$

The power optimality criterion developed by Murray leads to γ_{M} in (7). For the case of the LM-LAD-LCX bifurcation, these two equations are complemented with the mass conservation

$$Q_{\mathrm{LM}} = Q_{\mathrm{LAD}} + Q_{\mathrm{LCX}} \tag{8}$$

Introducing expressions (7) into (8) we obtain the constant σ, that is

$$\sigma = \frac{Q_{\mathrm{LM}}}{D_{\mathrm{LAD}}^{\gamma} + D_{\mathrm{LCX}}^{\gamma}} \tag{9}$$

and characterize the flow splitting at the bifurcation

$$Q_{\mathrm{A}} = \frac{D_{\mathrm{A}}^{\gamma}}{D_{\mathrm{LAD}}^{\gamma} + D_{\mathrm{LCX}}^{\gamma}} Q_{\mathrm{LM}} \quad \mathrm{A} \in \{\mathrm{LAD}, \mathrm{LCX}\}. \tag{10}$$

If we assume that the peripheral resistance fully determines the pressure drop (this is reasonable because we are analyzing a small portion of the arterial network), we can write

$$Q_{\mathrm{A}} = \frac{P_{\mathrm{LM}} - P_v}{R_{\mathrm{A}}} \quad \mathrm{A} \in \{\mathrm{LAD}, \mathrm{LCX}\} \tag{11}$$

where $P_{\mathrm{LM}} - P_v$ is the pressure drop between the aortic root and the venous return (in this work $P_{\mathrm{LM}} - P_v = 90$ mmHg). Hence, with (9) into (10), we characterize the resistances R_{LAD} and R_{LCX} used in (4) as follows

$$R_{\mathrm{A}} = \frac{(P_{\mathrm{LM}} - P_v)(D_{\mathrm{LAD}}^{\gamma} + D_{\mathrm{LCX}}^{\gamma})}{Q_{\mathrm{LM}}} D_{\mathrm{A}}^{-\gamma} \quad \mathrm{A} \in \{\mathrm{LAD}, \mathrm{LCX}\} \tag{12}$$

Observe that different exponents define different blood flow simulations through different peripheral resistances, which are denoted $R_{\mathrm{A}}^{\mathrm{C}}$, $\mathrm{A} \in \{\mathrm{LAD}, \mathrm{LCX}\}$, $\mathrm{C} \in \{\mathrm{M}, \mathrm{HK}, \mathrm{GS}, \mathrm{SS}\}$. Murray and Huo-Kassab exponents, $\gamma_{\mathrm{M}} = 3$ and $\gamma_{\mathrm{HK}} = 7/3$, are the same for all geometric models (both are one-fits-all approaches). The geometric-specific (GS) law implies finding γ_{GS} such that (1) holds for each specific patient. Finally, in the simulation-specific (SS) law we seek for the value of γ_{SS} such that

$$\mathrm{WSS}_{\mathrm{LAD}} = \mathrm{WSS}_{\mathrm{LCX}} \tag{13}$$

where $\mathrm{WSS}_{\mathrm{A}}$ is the spatially averaged wall shear stress magnitude in the endothelial wall of the A vessel, $\mathrm{A} \in \{\mathrm{LAD}, \mathrm{LCX}\}$, that is

$$\mathrm{WSS}_{\mathrm{A}} = \frac{1}{|\partial\Omega_{\mathrm{A}}|} \int_{\partial\Omega_A} |\tau_{\mathrm{A}}| d\partial\Omega \quad \mathrm{A} \in \{\mathrm{LAD}, \mathrm{LCX}\}, \tag{14}$$

where τ_{A} is the wall shear stress vector field over the corresponding endothelium $\partial\Omega_{\mathrm{A}}$, whose measure is $|\partial\Omega_{\mathrm{A}}|$, $\mathrm{A} \in \{\mathrm{LAD}, \mathrm{LCX}\}$, computed from the velocity field $\mathbf{u}$ solution of (4). The endothelial boundaries used for the calculation of the WSS are highlighted in color in Figure 2.

To find γ_{SS} we initially solve (4) with the boundary conditions given by $R^{\text{M}}_{\text{LAD}}, R^{\text{M}}_{\text{LCX}}$.

Then, we modify these resistances iteratively until (13) is verified up to a given tolerance (tol $= 0.001$).

To find γ_{SS} we proceed iteratively as follows: set initial guess resistances as $R^0_{\text{LAD}} = R^{\text{M}}_{\text{LAD}}$, $R^0_{\text{LCX}} = R^{\text{M}}_{\text{LCX}}$, then

for $k = 0, 1, 2, \ldots,$ do

using $(R^k_{\text{LAD}}, R^k_{\text{LCX}})$ solve (6) to obtain $(\mathbf{u}^{k+1}, p^{k+1}, \lambda^{k+1}_{\text{LM}})$,

compute $(\text{WSS}^{k+1}_{\text{LAD}}, \text{WSS}^{k+1}_{\text{LCX}})$ with (14),

compute $\theta^{k+1} = \dfrac{1}{2}\left(1 + \dfrac{\text{WSS}^{k+1}_{\text{LCX}}}{\text{WSS}^{k+1}_{\text{LAD}}}\right)$,

if $\theta^{k+1} = 1$ then exit algorithm,

if $\theta^{k+1} > 1$ then $R^{k+1}_{\text{LAD}} = (2 - \theta^{k+1}) R^k_{\text{LAD}}$,

if $\theta^{k+1} < 1$ then $R^{k+1}_{\text{LAD}} = \theta^{k+1} R^k_{\text{LAD}}$,

compute $R^{k+1}_{\text{LCX}} = \left(\dfrac{1}{R^{\text{M}}_{\text{LAD}}} + \dfrac{1}{R^{\text{M}}_{\text{LCX}}} - \dfrac{1}{R^{k+1}_{\text{LAD}}}\right)^{-1}$,

until $\dfrac{|\text{WSS}^{k+1}_{\text{LAD}} - \text{WSS}^{k+1}_{\text{LCX}}|}{\text{WSS}^{k+1}_{\text{LAD}}} < \epsilon$,

with $\epsilon = 0.001$. Note that the equivalent resistance is the same at all iterations.

This iterative procedure yields the *optimal* resistances $R^{\text{SS}}_{\text{LAD}}, R^{\text{SS}}_{\text{LCX}}$. Thus, the value of γ_{SS} is found through the ratio of both expressions (12), leading to

$$\frac{R^{\text{SS}}_{\text{LAD}}}{R^{\text{SS}}_{\text{LCX}}} = \left(\frac{D_{\text{LCX}}}{D_{\text{LAD}}}\right)^{\gamma_{\text{SS}}}, \tag{15}$$

and so

$$\gamma_{\rm SS} = \frac{\log\left(\frac{R_{\rm LAD}^{\rm SS}}{R_{\rm LCX}^{\rm SS}}\right)}{\log\left(\frac{D_{\rm LCX}}{D_{\rm LAD}}\right)}. \tag{16}$$

Expression (16) is singular for $D_{\rm LAD} = D_{\rm LCX}$, which implies that, under the hypotheses considered, (13) holds regardless the value of $\gamma_{\rm SS}$. This is not exactly true in practice because we are solving problem (4) and the hypotheses are not exactly verified. Out of the 50 patients, 2 featured nearly the same LAD and LCX diameters, and were removed in the analysis corresponding to the simulation-specific scenario.

In the same way expression (2) measures the geometric deviation at the patient level, we also define the functional index

$$\mathsf{F}_{\rm A}^{\rm C} = \frac{{\rm WSS}_{\rm A}^{\rm C}}{{\rm WSS}_{\rm A}^{\rm SS}} \qquad {\rm A} \in \{{\rm LAD}, {\rm LCX}\}, \ {\rm C} \in \{{\rm M}, {\rm HK}, {\rm GS}\}, \tag{17}$$

which measures the deviation of the wall shear stress in each vessel from the optimal scenario in which these stresses are perfectly balanced between LAD and LCX (situation given by the SS scenario). Also, we define the LAD/LCX WSS balancing index

$$\mathsf{B}^{\rm C} = \frac{{\rm WSS}_{\rm LAD}^{\rm C}}{{\rm WSS}_{\rm LCX}^{\rm C}} \qquad {\rm C} \in \{{\rm M}, {\rm HK}, {\rm GS}\}. \tag{18}$$

3. Results

The exponents of the different power laws investigated in this work are reported in Figure 3(a). Geometric-specific and simulation-specific power laws imply in an exponent γ which is specific for each case. For the geometric-specific law, we obtained ($n = 50$): $\gamma_{\rm GS} = 2.32 \pm 1.05$, range $[1.03, 7.40]$, and median (IQR) of $2.03(1.68, 2.87)$. A gamma distribution was used to fit $\gamma_{\rm GS}$, yielding parameters $a = 6.90, b = 0.34$, see Figure 3(b). In turn, the simulation-specific law ($n = 48$, two cases removed because $D_{\text{LAD}} = D_{\text{LCX}}$) rendered an exponent $\gamma_{\text{SS}} = 2.62 \pm 0.64$, range $[1.05, 6.36]$, and median (IQR) of $2.59(2.41, 2.74)$. The gamma distribution used to fit γ_{SS} resulted in parameters $a = 22.16, b = 0.12$, see Figure 3(c).

Law	γ
M	3
HK	7/3
GS	$2.32 \pm 1.07^{*}$
SS	$2.62 \pm 0.64^{+}$

(a)

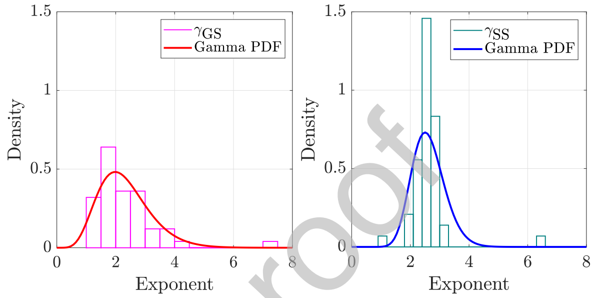

(b) (c)

Figure 3: Left: Table summarizing the analyzed allometric laws. Murray's (M) and Huo-Kassab' (HK) laws are power laws with a well-defined exponent. Geometry-specific (GS) law is the power law constructed using the diameters obtained from the image analysis (*: computed from image data, see Results section). Simulation-specific (SS) law is the power law constructed from the simulation in which the WSS is matched in both branching vessels (+: computed from simulation data, see Results section). Right: Distributions of exponents γ_{GS} and γ_{SS} from the entire sample. A Gamma distribution is used to approximate the data.

Figure 4 features the correlation plot between the measured diameter (horizontal axis) and the diameter predicted by the power law (1) (vertical axis), where the exponent γ is either γ_{M}, γ_{HK}, or γ_{SS}. The three plots are generated considering: (a) $D_{\text{LAD}}, D_{\text{LCX}}$ as given data to predict D_{LM} using (1), (b) $D_{\text{LM}}, D_{\text{LAD}}$ as given data to predict D_{LCX} using (1), and (c) $D_{\text{LM}}, D_{\text{LCX}}$ as given data to predict D_{LAD} using (1). Correlation coefficients are also reported in these plots. Power law with Murray coefficient rendered the better correlation coefficient between predicted and measured vessel diameters.

Figure 5 shows the geometric and optimality measures, R and F respectively. The violin plots in Figure 5(a) and Figure 5(b) illustrate the distribution of the discrepancy measures around the theoretical value of 1. A different visualization is shown in the R vs. B plot from Figure 5(c). These figures confirm that the

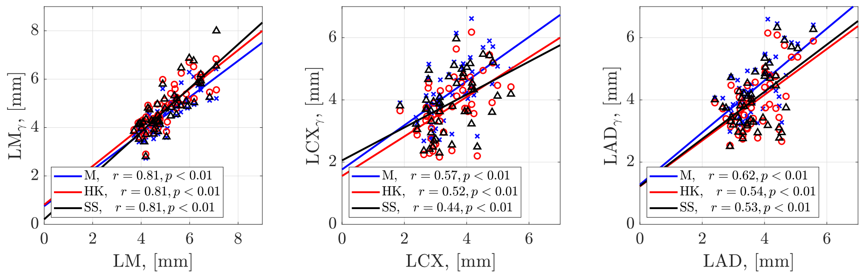

(a) (b) (c)

Figure 4: Correlation plots between measured vessel diameter and prediction using the different allometric laws (M: Murray, HK: Huo-Kassab, SS: simulation-specific). (a) data: $D_{\mathrm{LAD}}, D_{\mathrm{LCX}}$, prediction: D_{LM}, (b) data: $D_{\mathrm{LM}}, D_{\mathrm{LAD}}$, prediction: D_{LCX}, (c) data: $D_{\mathrm{LM}}, D_{\mathrm{LCX}}$, prediction: D_{LAD}.

GS scenario yields perfect $\mathsf{R}_{\mathrm{GS}} = 1$, while the simulation-specific scenario gives $\mathsf{B}_{\mathrm{SS}} = 1$.

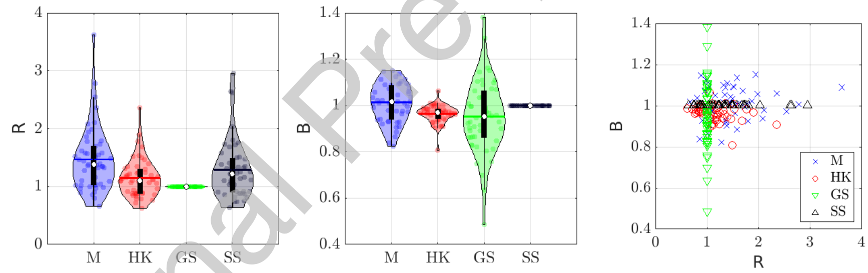

(a) (b) (c)

Figure 5: Geometric (R) and balancing (B) measures of the performance of each power law for the different scenarios: M: Murray, HK: Huo-Kassab, GS: geometry specific (such that (1) holds), SS: simulation-specific (such that (13) holds).

Table 2 provides the statistics for the geometric and functional measures introduced here. Figure 6 displays the distribution of the functional indexes that measure the discrepancy in the WSS with respect to the baseline SS scenario in both LAD and LCX. Figure 6(a) and Figure 6(b) present the violin plots for the discrepancy with respect to the SS scenario, as measured by the functional index F for the LAD and LCX, respectively. Figure 6(c) shows the inverse relation existing between these two indexes.

Index	Law (C)	mean ± std	[min, max]	median (IQR)
R_{C}	M	1.47 ± 0.55	[0.66, 3.62]	1.38 (1.03, 1.70)
	HK	1.15 ± 0.33	[0.62, 2.36]	1.10 (0.88, 1.30)
	GS	1.00 ± 0.00	[1.00, 1.00]	1.00 (1.00, 1.00)
	SS	1.29 ± 0.50	[0.64, 2.96]	1.22 (0.91, 1.49)
B^{C}	M	1.01 ± 0.08	[0.82, 1.15]	1.02 (0.94, 1.09)
	HK	0.96 ± 0.04	[0.81, 1.06]	0.97 (0.94, 0.98)
	GS	0.95 ± 0.16	[0.49, 1.38]	0.95 (0.86, 1.06)
	SS	1.00 ± 0.00	[1.00, 1.00]	1.00 (1.00, 1.00)
$\mathsf{F}^{\mathrm{C}}_{\mathrm{LAD}}$	M	1.00 ± 0.04	[0.87, 1.05]	1.01 (0.97, 1.03)
	HK	0.99 ± 0.01	[0.95, 1.04]	0.99 (0.98, 0.99)
	GS	0.98 ± 0.07	[0.80, 1.12]	0.98 (0.94, 1.03)
$\mathsf{F}^{\mathrm{C}}_{\mathrm{LCX}}$	M	0.99 ± 0.04	[0.89, 1.07]	0.99 (0.95, 1.03)
	HK	1.02 ± 0.03	[0.98, 1.18]	1.02 (1.01, 1.04)
	GS	1.05 ± 0.13	[0.80, 1.71]	1.03 (0.97, 1.09)

Table 2: Statistics for the indexes that measure the geometric and functional behavior of the left main coronary bifurcation. R: Murray ratio, see (2); F: functional index, see (17); B: balancing index, see (18). These indexes are reported for the different laws, M: Murray, HK: Huo-Kassab, GS: geometric-specific, SS: simulation-specific. IQR stands for interquartile range.

In Figure 7 we report the analysis of the results as a function of the asymmetry ratio ζ. We can see that the distribution of the asymmetry ratio is around 1. The Murray ratio R is mildly negatively correlated with ζ, and this correlation is not statistically significant (see Figure 7(a)). For the functional indexes $\mathsf{F}_{\mathrm{LAD}}$ and $\mathsf{F}_{\mathrm{LCX}}$, the correlation with Murray and Huo-Kassab is high, as expected because we are using these rules to define the boundary conditions. In turn, the dispersion of the indexes in the geometric-specific scenario is larger, and is more similar to the Huo-Kassab law, but the correlation in the data is only mild, as seen in Figures 7(b) and 7(c).

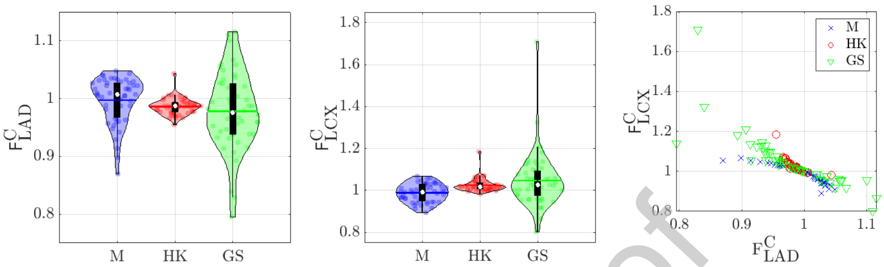

(a) (b) (c)

Figure 6: Indexes $\mathsf{F}_{\mathrm{LAD}}$ (left) and $\mathsf{F}_{\mathrm{LCX}}$ (right) (see (17)) characterizing the relation of wall shear stress (WSS) in the LAD and LCX for the different scenarios (M, HK, GS) with respect to the WSS-balanced SS setting.

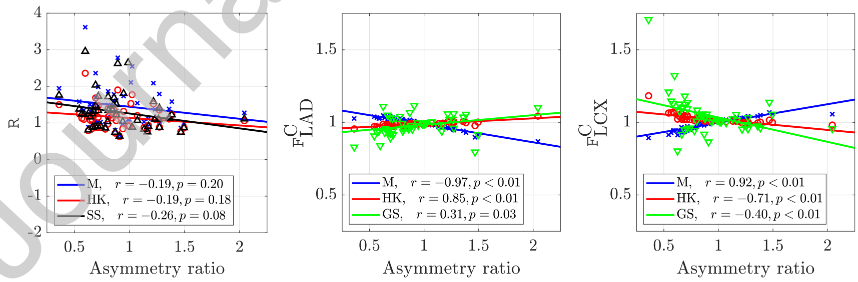

(a) (b) (c)

Figure 7: Results as a function of the asymmetry ratio ζ. Murray index R (left), and indexes $\mathsf{F}_{\mathrm{LAD}}$ (middle) and $\mathsf{F}_{\mathrm{LCX}}$ (right) (see (17)), for the different scenarios (M, HK, GS), as a function of the asymmetry ratio ζ.

4. Discussion

4.1. Main findings

We investigated the anatomical features of the left main coronary bifurcation, and employed computer simulation to estimate the wall shear stresses in the daughter vessels using a set of 50 patients featuring angiographically normal coronary arteries (free from obstructive disease). The study focused on the role of power laws to describe arterial branching, its relation with flow splitting and the impact on the shear stresses acting over the endothelium. Particularly, we compared conventional power laws with geometric-specific and simulation-specific power laws.

Compared to one-fits-all approaches, such as the Murray exponent $\gamma_{\mathrm{M}} = 3$ and the Huo-Kassab exponent $\gamma_{\mathrm{HK}} = 7/3 = 2.33$, from the geometric analysis of the main bifurcation in the coronary tree ($\gamma_{\mathrm{GS}} = 2.32 \pm 1.07$) we conclude that, in average, the HK law is the one that better described the observed vessel diameters. Even though, from all the laws studied, the one that featured a more compact distribution of the Murray ratio (see (2)) is the HK law, as seen in Figure 5(a). This finding is at odds with the fact that Murray exponent proved to yield better correlation between predicted and measured vessel diameter once a couple of vessel diameters are known, implying that a better correlation does not necessarily imply better geometric and hemodynamic features.

Another important observation is the fact that the perfect Murray ratio R between LM and LAD/LCX vessel diameters counteracts the perfect WSS balance between LAD and LCX, resulting in a significant spread in the functional index B (see (18) and see Figure 5(b)). Note that the flow splitting dictated by a perfect geometric bifurcation in the sense of the perfect Murray ratio, i.e. $\mathsf{R} = 1$, is far from ensuring perfect WSS balance, i.e. $\mathsf{B} = 1$, between the daughter vessels. The Murray law is the approach that, in average, offers the best balancing index (see Table 2). However, the distribution is wide, and it turns out that the HK law results in a trade-off between geometry and functionality, as observed in Figure 5(c), and confirmed by the statistics in Table 2. This is crucial for hemodynamic simulation settings, as most of the works in the literature rely on some sort of power law fed with the patient's vessel diameters. Such observation can be explained by the fact that the flow splitting is governed by microvascular peripheral resistance, whose allometric law is certainly different from the power law observed in the along vessel generations. In [33], the authors reported that the average exponent actually varies, along network depth, in the ranges $(1.3, 3)$, $(1.7, 2.7)$, and $(0.1, 7.2)$ for different territories in the cerebral vasculature. In the present study, we have seen that even such apparently small variability could lead to important deviations in the LAD/LCX WSS balance. From all the laws investigated, again the HK law is the one that featured more balanced LAD/LCX endothelial stresses provoked by the action of blood flow. Again, the conclusion drawn from this observation is that the HK law is more compliant with the precept that the arterial tree is continuously adapting to maintain homogeneous WSS values across the arterial tree [34, 35].

Exploiting the simulation-specific (SS) scenario, in which the WSS is perfectly balanced between LAD and LCX, as a reference solution, we can observe the relative impact of considering the Murray, the Huo-Kassab and the geometry-specific exponents. Relative to the SS case, the WSS delivered by the HK power law resulted in a more compact and symmetric distribution, while the Murray and the geometry-specific exponents rendered skewed distributions for both LAD and LCX (see Figure 6 and also the statistics in Table 2). Moreover, we note that the Murray scenario yielded the mean value which is closest to the reference one. However, this is not compensated by the wider distribution compared to the HK law. The negative correlation observed between the relative deviation of the WSS in the LAD and in the LCX with respect to the SS scenario is explained by the fact that the flow rate into the left main vessel is ensured to be the same for all cases, enforcing the same Reynolds number, and the same flow regime for all the scenarios (M, HK, GS, SS).

From the analysis of the strategies proposed in this study, it is also interesting to highlight the possibility of generalizing the branching power law. A possible approach to doing that based on geometry, is to expand the power law by adding a parameter depending. Here, we assessed the dependence of the branching models with the asymmetry ratio [25]. The functional index in the geometric-specific scenario showed only a mild correlation with the asymmetry ratio. Interestingly, the correlation was close to that featured by the Huo-Kassab branching rule.

The downside of the SS scenario is the need for performing three-dimensional simulations, which may be costly for large vascular models. With the advent of machine learning algorithms a by-product of the present study could be the generation of ground truth data (the flow splitting ratio obtained in the SS scenario), to train and validate learning algorithms. Such learned branching laws (or flow-splitting rules) may become more accurate regarding the homogeneity of WSS among vessels. This is left as future work, and as a potential application of the core ideas introduced in this study.

The present study focused on the left main bifurcation and on idealized tubular geometries. Although the extrapolation of the present findings to downstream bifurcations could be a common practice, it should be subjected to scrutiny in view of the variability of bifurcation exponents with network depth [33]. The use of realistic vascular geometries to investigate the impact of branching laws on the WSS, and the construction of physics-driven boundary conditions based on geometric considerations is still an open problem. Indeed, the multiple outlet problem may not have a solution if we seek for the BCs such that the WSS is the same in all branches. Therefore, the present study may not be replicable in realistic geometries with many outlets. Definitely, this problem of defining outlet boundary conditions will continue to deserve attention from the community.

4.2. Limitations

The geometric models employed in the analysis do not take into account the real arterial geometry, but it is a phantom model built from vessel diameter data. Assembling a large patient dataset is challenging. Large studies including multi-modality imaging do not include simulation [21]. The utilization of simulation techniques to provide functional insight about blood flow on top of geometry solely posits several challenges, because of the cost involved in the numerical simulations and in the management of input/output data processing. Here we employed an efficient numerical approach that enables the study of hundreds of simulations. Analyzing the effect of the different scenarios proposed in realistic geometries and also comparing control and diseased patients is out of the scope of this paper and should be addressed in the future.

The blood flow model is steady-state, in contrast to the pulsatile conditions of coronary blood flow. Even if this is a rather simplifying hypothesis, observe that Murray's law was also conceived under steady-state conditions. Thus, in this work we preferred to focus on the more fundamental question about the criterion to determine the flow splitting, instead of the hypotheses underlying the blood flow model. Moreover, concerning the computation of average WSS, there is evidence that steady-state models possess great predictive capabilities compared to the ground truth solution given by time-dependent models [28, 36, 29].

Patient-specific coronary flow rate measurements were not available, so we considered the same flow rate prescribed at the inlet of the bifurcation, where the value depended solely on arterial dominance. Inter-individual variability can be large concerning the myocardial flow supply. Nevertheless, note that the Reynolds number in the coronary circulation is not large, and so we expect this assumption is not influential for the analysis based on the average of WSS. The same may not hold for maximum values and even oscillatory behavior of the WSS, which were not analyzed in the present study.

Another limitation is that we restricted our analysis to the main left bifurcation, regardless the number of vessels downstream the LAD and LCX. Complementary research should consider an extended vascular domain.

5. Final Remarks

Large anatomical variability is a normal feature of arterial morphology, both in diseased and control patients, which allows us to conclude that macrovascular branching patters cannot be used to solely explain pathology. Moreover, based on the principle that the wall shear stress tends to be homogeneous across the different scales in the circulation, a power law formula calibrated with patient-specific branching data does a disservice to dictating the flow rate splitting in mathematical models, under the hypothesis for the flow-diameter relationship considered here. The proposed approach to define peripheral resistances such that the endothelial shear stresses in both LAD and LCX are the same showed us that from all the studied laws, the Huo-Kassab power law stands out as the one that renders less heterogeneity in the wall shear stresses, when comparing LAD to LCX.

Conflicts of Interest

None

Funding

This work was partially supported by the Brazilian agencies CNPq (grant numbers 301224/2016-1 and 407751/2018-1), and FAPESP (grant numbers 2014/50889-7 and 2018/14221-2). Also by Argentinean agency ANPCyT, grant number PICT-2018-02427.

Ethical Approval

This project was revised and approved by the Local Ethics Committee.

References

[1] M. Friedman, O. Deters, F. Mark, C. Brent Bargeron, G. Hutchins, Arterial geometry affects hemodynamics. a potential risk factor for atherosclerosis, Atherosclerosis 46 (2) (1983) 225–231.

[2] M. Friedman, O. Deters, C. Bargeron, G. Hutchins, F. Mark, Shear-dependent thickening of the human arterial intima, Atherosclerosis 60 (1986) 161–171.

[3] M. Friedman, P. Baker, Z. Ding, B. Kuban, Relationship between the geometry and quantitative morphology of the left anterior descending coronary artery, Atherosclerosis 125 (2) (1996) 183–192.

[4] H. Zhu, M. Friedman, Relationship between the dynamic geometry and wall thickness of a human coronary artery, Arteriosclerosis, Thrombosis, and Vascular Biology 23 (12) (2003) 2260–2265.

[5] C. White, C. Wright, D. Doty, L. Hiratza, C. Eastham, D. Harrison, M. Marcus, Does visual interpretation of the coronary arteriogram predict the physiologic importance of a coronary stenosis?, New England Journal of Medicine 310 (13) (1984) 819–824.

[6] S. Pant, N. Bressloff, G. Limbert, Geometry parameterization and multidisciplinary constrained optimization of coronary stents, Biomechanics and Modeling in Mechanobiology 11 (1-2) (2012) 61–82.

[7] A. Garca, E. Pea, M. Martnez, Influence of geometrical parameters on radial force during self-expanding stent deployment. application for a variable radial stiffness stent, Journal of the Mechanical Behavior of Biomedical Materials 10 (2012) 166–175.

[8] L. Ellwein, D. Marks, R. Migrino, W. Foley, S. Sherman, J. LaDisa, J.F., Image-based quantification of 3d morphology for bifurcations in the left coronary artery: Application to stent design, Catheterization and Cardiovascular Interventions 87 (7) (2016) 1244–1255.

[9] C. A. Taylor, T. A. Fonte, J. K. Min, Computational Fluid Dynamics Applied to Cardiac Computed Tomography for Noninvasive Quantification of Fractional Flow Reserve, Journal of the American College of Cardiology 61 (22) (2013) 2233–2241.

[10] J. K. Min, J. Leipsic, M. J. Pencina, D. S. Berman, B.-K. Koo, C. van Mieghem, A. Erglis, F. Y. Lin, A. M. Dunning, P. Apruzzese, M. J. Budoff, J. H. Cole, F. A. Jaffer, M. B. Leon, J. Malpeso, G. B. J. Mancini, S.-J. Park, R. S. Schwartz, L. J. Shaw, L. Mauri, Diagnostic Accuracy of Fractional Flow Reserve From Anatomic CT Angiography, JAMA 308 (12) (2012) 1237.

[11] C. Murray, The physiological principle of minimum work applied to the angle of branching of arteries, Journal of General Physiology 9 (6) (1926) 835–841.

[12] M. Zamir, Optimality principles in arterial branching, Journal of Theoretical Biology 62 (1) (1976) 227–251.

[13] C. Seiler, R. Kirkeeide, K. Gould, Basic structure-function relations of the epicardial coronary vascular tree: Basis of quantitative coronary arteriography for diffuse coronary artery disease, Circulation 85 (6) (1992) 1987–2003.

[14] Y. Zhou, G. Kassab, S. Molloi, On the design of the coronary arterial tree: A generalization of murray's law, Physics in Medicine and Biology 44 (12) (1999) 2929–2945.

[15] S. Lorente, W. Wechsatol, A. Bejan, Tree-shaped flow structures designed by minimizing path lengths, International Journal of Heat and Mass Transfer 45 (16) (2002) 3299–3312.

[16] B. Masters, Fractal analysis of the vascular tree in the human retina, Annual Review of Biomedical Engineering 6 (2004) 427–452.

[17] B. Guerciotti, C. Vergara, S. Ippolito, A. Quarteroni, C. Antona, R. Scrofani, Computational study of the risk of restenosis in coronary bypasses, Biomechanics and Modeling in Mechanobiology 16 (1) (2017) 313–332.

[18] N. P. Smith, A. J. Pullan, P. J. Hunter, Generation of an anatomically based geometric coronary model, Annals of biomedical engineering 28 (1) (2000) 14–25.

[19] S. Di Gregorio, M. Fedele, G. Pontone, A. Corno, P. Zunino, C. Vergara, A. Quarteroni, A computational model applied to myocardial perfusion in the human heart: From large coronaries to microvasculature, Journal of Computational Physics 424 (2021) 109836.

[20] A. van der Giessen, H. Groen, P.-A. Doriot, P. de Feyter, A. van der Steen, F. van de Vosse, J. Wentzel, F. Gijsen, The influence of boundary conditions on wall shear stress distribution in patients specific coronary trees, Journal of Biomechanics 44 (6) (2011) 1089–1095.

[21] A. Schoenenberger, N. Urbanek, S. Toggweiler, R. Seelos, P. Jamshidi, T. Resink, P. Erne, Deviation from murray's law is associated with a higher degree of calcification in coronary bifurcations, Atherosclerosis 221 (1) (2012) 124–130.

[22] L. Mller, F. Fossan, A. Brten, A. Jrgensen, R. Wiseth, L. Hellevik, Impact of baseline coronary flow and its distribution on fractional flow reserve pre-

diction, International Journal for Numerical Methods in Biomedical Engineering (2019) e3246.

[23] S. Sankaran, H. Kim, G. Choi, C. Taylor, Uncertainty quantification in coronary blood flow simulations: Impact of geometry, boundary conditions and blood viscosity, Journal of Biomechanics 49 (12) (2016) 2540–2547.

[24] Y. Huo, G. Finet, T. Lefvre, Y. Louvard, I. Moussa, G. Kassab, Optimal diameter of diseased bifurcation segment: A practical rule for percutaneous coronary intervention, EuroIntervention 7 (11) (2012) 1310–1316.

[25] M. Olufsen, Structured tree outflow condition for blood flow in larger systemic arteries, American Journal of Physiology - Heart and Circulatory Physiology 276 (1 45-1) (1999) H257–H268.

[26] P. Medrano-Gracia, J. Ormiston, M. Webster, S. Beier, A. Young, C. Ellis, C. Wang, Ö. Smedby, B. Cowan, A computational atlas of normal coronary artery anatomy., EuroIntervention: journal of EuroPCR in collaboration with the Working Group on Interventional Cardiology of the European Society of Cardiology 12 (7) (2016) 845–854.

[27] L. MansillaAlvarez, P. Blanco, C. Bulant, E. Dari, A. Veneziani, R. Feijo, Transversally enriched pipe element method (TEPEM): An effective numerical approach for blood flow modeling, International Journal for Numerical Methods in Biomedical Engineering 33 (4) (2017) e2808.

[28] C. Bulant, P. Blanco, G. Maso Talou, C. Guedes Bezerra, P. Lemos, R. Feijóo, A head-to-head comparison between CCTA- and IVUS-derived coronary blood flow models, Journal of Biomechanics 51 (2017) 65–76.

[29] F. Fossan, J. Sturdy, L. Müller, A. Strand, A. Bråten, A. Jorgensen, R. Wiseth, L. Hellevik, Uncertainty quantification and sensitivity analysis

for computational ffr estimation in stable coronary artery disease, Cardiovascular Engineering and Technology 9 (4) (2018) 597–622.

[30] L. Formaggia, J.-F. Gerbeau, F. Nobile, A. Quarteroni, Numerical treatment of defective boundary conditions for the navier-stokes equations, SIAM Journal on Numerical Analysis 40 (1) (2002) 376–401.

[31] A. Veneziani, C. Vergara, Flow rate defective boundary conditions in haemodynamics simulations, International Journal for Numerical Methods in Fluids 47 (8-9) (2005) 803–816.

[32] S. Sakamoto, S. Takahashi, A. U. Coskun, M. I. Papafaklis, A. Takahashi, S. Saito, P. H. Stone, C. L. Feldman, Relation of Distribution of Coronary Blood Flow Volume to Coronary Artery Dominance, The American Journal of Cardiology 111 (10) (2013) 1420–1424.

[33] F. Mut, S. Wright, G. Ascoli, J. Cebral, Morphometric, geographic, and territorial characterization of brain arterial trees, International Journal for Numerical Methods in Biomedical Engineering 30 (7) (2014) 755–766.

[34] A. Pries, T. Secomb, P. Gaehtgens, Design principles of vascular beds, Circulation Research 77 (5) (1995) 1017–1023.

[35] L. Taber, An optimization principle for vascular radius including the effects of smooth muscle tone, Biophysical Journal 74 (1) (1998) 109–114.

[36] P. D. Morris, D. A. Silva Soto, J. F. Feher, D. Rafiroiu, A. Lungu, S. Varma, P. V. Lawford, D. R. Hose, J. P. Gunn, Fast virtual fractional flow reserve based upon steady-state computational fluid dynamics analysis 2 (4) (2017) 434–446.

Conflicts of Interest

None declared